

Physics-based simulations of grassfire propagation on sloped terrain at field scale: flame dynamics, mode of fire propagation and heat fluxes[†]

Jasmine Innocent^{A,B}, Duncan Sutherland^{B,C}, Nazmul Khan^{A,B}  and Khalid Moinuddin^{A,B,*}

For full list of author affiliations and declarations see end of paper

***Correspondence to:**

Khalid Moinuddin
Institute for Sustainable Industries and
Liveable Cities, Victoria University,
Melbourne, Australia
Email: Khalid.Moinuddin@vu.edu.au

ABSTRACT

The interaction of wind and fire on a sloped terrain is always complex owing to the mechanisms of heat transfer and flame dynamics. Heating of unburned vegetation by attached flames may increase the rate of spread. The relative intensities of convective and radiative heat fluxes may change fire behaviour significantly. This paper presents a detailed analysis of flame dynamics, mode of fire propagation and surface radiative and convective heat fluxes on sloped terrain at various wind speeds using physics-based simulations. It was found that with increasing slope angles and wind velocity, the plume inclines more towards the ground and becomes elongated in upslope cases, whereas in downslope cases, the plume rises from the ground earlier. For higher wind velocities, the flame and near-surface flame dynamics appear to show rising, even though the plume is attached. The flame contour results indicate that the near-surface flame dynamics are difficult to characterise using Byram's number. A power-law correlation was observed between the simulated flame lengths and fireline intensities. The convective heat fluxes are more relevant for wind-driven fire propagation and greater upslopes, whereas both fluxes are equally significant for lower driving wind velocities compared with higher wind velocities.

Keywords: Byram number, fire propagation, flame, grassfire, heat fluxes, plume, rate of spread (RoS), slope, wind velocity.

Introduction

In the preceding companion paper, the first part of this study, [Innocent *et al.* \(2022\)](#), we described the model set up, validation and the comparisons of the rate of spread (RoS) with existing empirical models. The current part focuses on flame dynamics, identifies the mode of fire propagation, and examines surface radiative and convective heat fluxes. The overarching aim of this study is to identify the limitations of current empirical fire spread models, with an eye toward incorporating more complex fire behaviour into empirical models in the future.

[Sharples *et al.* \(2011\)](#) highlighted the role of environmental factors such as the modification of fire weather conditions by topography, and coupling between terrain, fire and atmosphere, that can significantly affect the dynamic nature of fire propagation. This results in the potential for fire to propagate laterally along certain terrain elements such as slope ([Sharples *et al.* 2011](#)).

[Viegas \(2004\)](#) in their laboratory-scale experiments and [Dold and Zinoviev \(2009\)](#) in their laboratory- and field-scale experiments observed a rapid increase in RoS for fires burning on steep slopes, despite burning under constant environmental conditions. This rapid acceleration of fires has been termed 'fire blow-up' or 'fire eruption'. [Sharples \(2017\)](#) stated that eruptive behaviour occurs owing to an interaction between the slope of the terrain and the fire plume. According to [Sharples \(2017\)](#), for steep slopes, a

Received: 3 September 2021

Accepted: 5 December 2022

Published: 20 January 2023

Cite this:

Innocent J *et al.* (2023)
International Journal of Wildland Fire
doi:[10.1071/WF21125](https://doi.org/10.1071/WF21125)

© 2023 The Author(s) (or their employer(s)). Published by CSIRO Publishing on behalf of IAWF.

[†]Part 1 of this paper is available at *International Journal of Wildland Fire*, <https://doi.org/10.1071/WF21124>.

localised pressure deficit can form immediately upslope ahead of the fire, and this causes the flames and plume to attach to the terrain surface.

Dold and Zinoviev (2009) conducted a series of laboratory experiments (using a uniform layer of loosely packed straw as fuel) on upslope scenarios (15°, 20°, 25°, 30° and 35°) and a field experiment (40 × 25 m plot, at +23° slope) with straight-line fires in mild or negligible wind conditions. They observed eruptive growth of fire and flame attachment at a slope of 23° with the field experiment, and closer to 30° in the laboratory experiments. They found that for a low driving wind velocity (their experiments were conducted at a low ambient wind speed of $1.6 \pm 1 \text{ m s}^{-1}$), for fires burning above 20° slope, the interaction of wind and topographical effects (such as slope) can have significant implications for plume behaviour. This interaction notably affects heat transfer from the burning zone into unburnt fuel (Apte et al. 1991; Cobian-Iñiguez et al. 2019).

Mendes-Lopes et al. (2003), Dold and Zinoviev (2009), Dupuy and Maréchal (2011), Sharples (2017) and Sánchez-Monroy et al. (2019) in their separate studies with laboratory experiments observed that flame or plume attachment leads to enhanced preheating of fuels upslope ahead of the fire and resultant acceleration of the fire spread. If such phenomena occur, convective heat transfer significantly increases. It is therefore important to understand how and under which conditions plume and flame attachment behaviour occur.

Fire propagation is often characterised as either wind-driven mode or buoyancy-driven mode (Apte et al. 1991). Morvan and Frangieh (2018) analysed a large set of wildfire experimental data (both field and laboratory scale) from the literature to understand the role of RoS and wind velocity on fire propagation. They used Byram number, N_c , analysis to investigate the existence of two regimes of fire propagation (wind-driven fire vs plume-dominated fire) and hypothesised that heat transfer in buoyancy-driven fires is dominated by radiation, and by convection in wind-driven fires. This hypothesis is untested at large experimental scales; however, there are experimental measurements of heat fluxes in laboratory-scale fires (Dupuy and Maréchal 2011).

Characterising convective heating within flames is complex because the flames are highly non-steady (Finney et al. 2015). Finney et al. (2015) focused on the role of convective heating in wildfire spread. They conducted field experiments (stationary fire, with ~6 m flame length on 16-m wooden crib) and compared the results with laboratory-scale experimental studies in a wind tunnel facility. These experiments revealed that the structure and intermittency of flames that ignite fuel particles were correlated with instabilities induced by the strong buoyancy of the flame itself. They found that buoyancy generated by the fire induces vorticity and instabilities in the flame zone, and that controls the convective heating needed to ignite fuel particles and produce fire spread.

Mendes-Lopes et al. (2003) carried out a set of wind-tunnel experiments over a bed of *Pinus pinaster* needles with varying wind velocities of 0–3 m s^{-1} , fuel moisture contents of 10 and 18%, and slope angles of –15° to +15°. They analysed the flame parameters (flame length, height and angle) and RoS of both headfire and backing fire. They observed the strongest influence on RoS by far is wind velocity, followed by fuel moisture content, then slope. They also noted that the wind-driven flames bend over, increasing radiative heat transfer to the fuel, which is also heated by the convective heat transfer from the hot gases emanating from the flame. For upslope and wind-driven flames, the proximity of the flame and fuel due to the slope further increased heat transfer to the fuel bed.

Dupuy and Maréchal (2011) conducted laboratory fire experiments under no-wind conditions (in *Pinus halepensis* fuels beds) to understand the role of radiation and convection heat transfer on slopes on fire spread. In their experiments, they measured fuel and gas temperatures simultaneously at the same location (using an infrared camera and thermocouples, respectively) and measured the incident radiant heat flux received by a small fuel bed volume ahead of the fire line. These measurements were used to compute heat transfer for each slope angle (0°, 10°, 20° and 30°). Overall, they found radiative heating dominated the heat transfer mechanism on the slope between 0° and 20°, but close to the fire line (< 10 cm), the heat flux due to convective heating was also significant, reaching one-third of the net heat flux at 20° slope. When the slope angle increased from 20° to 30°, the RoS rose by a factor of 2.5 owing to a marked increase in convective heating, while radiative heat flux remained constant or decreased slightly (Dupuy and Maréchal (2011); this may be due to eruptive behaviour where the plume and flame attach to the slope (Sharples 2017). Based on the Byram number data and trend presented there, all the fires reported by Dupuy and Maréchal (2011) are likely buoyancy-driven fires.

Similar behaviour was observed by Sánchez-Monroy et al. (2019) in their laboratory-scale experiments, with a fuel bed of coarse excelsior heartwood, slopes ranging from –16° to +45° and no wind imposed, accompanied by numerical simulations using the physics-based model Wildland–urban interface Fire Dynamics Simulator (WFDS). They observed radiative heat transfer as the dominant mechanism of heating for slopes between 0° and +20°; however, for steep slopes of +31° and +45°, the convection heat transfer mechanism began to be relevant and became more important than the radiative heat flux term.

Morandini et al. (2018) conducted a series of laboratory fire spread experiments with no wind across a porous bed of excelsior with no slope and 30° upslope. They found that under no-slope conditions, preheating of the fuel particles was dominated by radiation from the flames, as expected from a buoyancy-driven fire. However, under 30° upslope conditions, they additionally observed a convective heat transfer mechanism that

resulted from the interaction between upstream air entrainment and the fire-generated buoyancy forces.

Chen *et al.* (2018) performed a series of laboratory-scale fire spread experiments on a pine needle board with $+5^\circ$ to $+30^\circ$ slopes under no-wind conditions. Fire spread rate and radiative heat flux were measured from the experiments along with flame parameters. The results showed a significant increase in flame length from $+20^\circ$ slope. For higher slope angles, the flame was observed to be tilted to the unburnt portion of the fuel bed owing to unbalanced air entrainment pushing the flame towards the unburned region. They noted that this behaviour intensified the radiative heat flux from the flame onto the fuel bed surface, leading to an increase in fire spread rate. However, they did not measure convective heat transfer. The flame attachment contributed significantly to increasing the fire spread rate for higher slope angles.

In the literature, experimentally, the aspects of flame dynamics and preheating of virgin fuels ahead of the fire front via heat fluxes related to surface fire on slopes have mostly been investigated at laboratory scale. In some studies, aspects were studied theoretically. Furthermore, the mode of fire propagation for these kinds of fires has not been investigated in detail.

Physics-based simulations have recently been established as an insightful and valid tool for studying wildfires (Mell *et al.* 2007; Moinuddin *et al.* 2018; Sánchez-Monroy *et al.* 2019; Sutherland *et al.* 2020). In the present study, we use WFDS (Mell *et al.* 2007; McGrattan *et al.* 2013) to investigate the combined effect of slope and wind on grassfire behaviour. These simulations can also be reliably used to investigate flame parameters, mode of fire propagation, and radiative and convective heat transfer processes. As the simulations presented here are a continuation of Part 1, Innocent *et al.* (2022), only a brief description of the

numerical methodology follows here; readers who are interested in the details of the simulation set-up, model reliability and accuracy, and the validation of the simulations should consult Moinuddin *et al.* (2018) and Innocent *et al.* (2022).

The simulated flame dynamics, mode of fire propagation and heat fluxes were analysed to answer the following questions:

- What effect does the driving wind velocity have on the flame parameters (plume and flame behaviour and flame length) and mode of fire propagation (wind-driven or buoyancy/plume-driven) as the slope angle varies?
- What are the relative contributions of radiative and convective heat transfer on sloped terrain at different driving wind velocities?

Simulation methodology

A rectangular domain of $360 \times 120 \times 60$ m, as shown in Fig. 1, was selected after conducting domain sensitivity tests. The burnable grass plot of dimensions 80×40 m was placed in the domain as shown and a 0.25 m grid size was used over the burnable region to ensure grid convergence (Innocent *et al.* 2022). For larger upslopes, $+30^\circ$, $+25^\circ$ at 12.5 m s^{-1} and $+30^\circ$ at 6 m s^{-1} , the simulations were repeated with a longer grass plot of 120×40 m section. The same thermo-physical and flammability properties as in Moinuddin *et al.* (2018) were used. A linear pyrolysis sub-model was adopted to model the thermal degradation of vegetation in a boundary fuel method, where ground vegetation is modelled like a porous solid with a thickness equal to the height of the vegetation. The slope was implemented by changing the components of the gravitational force in the X- and Z-directions. When the flow field was fully developed,

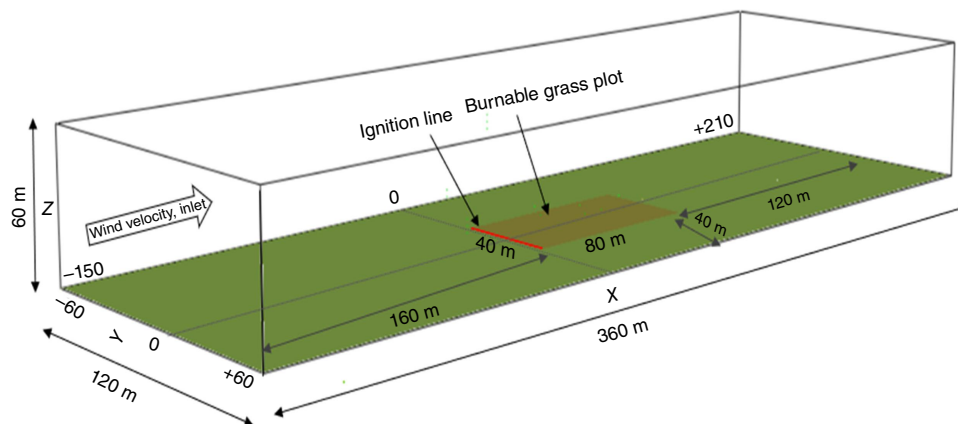


Fig. 1. The geometry of the domain: X, Y and Z dimensions are 360, 120 and 60 m, respectively. The geometric centre line axes $Y = 0$ and $X = 0$ are as shown in the figure. The burnable grass plot is 80×40 m (repeated with 120×40 m grass plot for greater upslopes ($+30^\circ$, $+25^\circ$ at 12.5 m s^{-1} and $+30^\circ$ at 6 m s^{-1})) (olive green region). At the inlet (YZ plane at $X = -150$), a wall of wind boundary condition is applied, which follows a $1/7$ power law (velocity vs height) with wind speeds of 12.5 , 6 and 3 m s^{-1} at 10 -m height. The 'open' boundary condition is applied at the top (XY plane at $Z = 60$ m) and outflow (YZ plane at $X = +210$ m) while symmetry boundary conditions are applied on both the left (ZX plane at $Y = -60$ m) and right side (ZX plane at $Y = +60$ m) of the domain. The bottom (XY plane at $Z = 0$) is considered the solid ground.

a prescribed line fire of 1000 kW m^{-2} was used as the ignition fire. The ignition fire was 40 m wide and 1 m deep, aligned with the leading edge of the burnable grass width as shown in Fig. 1. Further details of the model implementation, model reliability and accuracy, grid, ignition intensity and domain sensitivity studies can be found in Innocent et al. (2022).

Simulations were conducted at field scale for both upslopes and downslopes (-30° to $+30^\circ$) with varying U_{10} (open wind speed at 10 m above the ground) of 12.5, 6 and 3 m s^{-1} at the domain inlet (corresponding to 11.9, 5.6 and 2.8 m s^{-1} , respectively, prior to the ignition line). Table 1 lists the simulations conducted in this study for different slopes and driving wind velocities. Thermo-physical, pyrolysis and combustion parameters of vegetation and other input parameters used in the simulations are detailed in Table S1 of Supplementary Appendix A.

Results and discussion

Plume and flame dynamics

To visualise the plume contours, the instantaneous temperature slice output files obtained from the simulations were analysed using the numeric computing software Matlab (Davis and Sigmon 2005). The temperature slice data were obtained along the geometric centreline of the burnable grass plot and temperature contours for all cases were extracted at approximately the same instant of time, 30 s after ignition ($\pm 1 \text{ s}$ variation). This study acknowledges that fire behaviour can vary as the fire progresses. Caution needs to be taken in interpreting these plots because they

Table 1. List of simulations.

Slope angle	Simulation abbreviation	Driving wind velocity (m s^{-1})		
		12.5 m s^{-1}	6 m s^{-1}	3 m s^{-1}
-30°	Downslope 30	√	√	√
-25°	Downslope 25	√		
-20°	Downslope 20	√	√	√
-15°	Downslope 15	√		
-10°	Downslope 10	√	√	√
-5°	Downslope 5	√		
0°	Noslope	√	√	√
$+5^\circ$	Upslope 5	√		
$+10^\circ$	Upslope 10	√	√	√
$+15^\circ$	Upslope 15	√		
$+20^\circ$	Upslope 20	√	√	√
$+25^\circ$	Upslope 25	√ ^A		
$+30^\circ$	Upslope 30	√ ^A	√ ^A	√

^ARepeated with a longer burnable grass plot (extended to 120 m in the X-direction).

represent indicative plume behaviour of the turbulent flow at that instant. This instant in time was selected after cautious examination as being a broadly representative of the fields that reflect the finest graphic representation of plume attachment and rising behaviour for the cases presented.

The temperature contours (representing plumes) are plotted in Fig. 2, at the same instant in time, as the fire moves through the burnable grass plot in the X-direction, from a number of simulations. The plume is shown by colour shading that represents air temperature in degrees Kelvin, with the same temperature scale (indicated in the colour bar) for the same wind speed cases. Plumes (instantaneous) emanating from the fire front for 0° , $+10^\circ$, $+20^\circ$ and $+30^\circ$ upslopes at wind velocity 12.5 m s^{-1} are shown in Fig. 2a–d; and at 3 m s^{-1} are shown in Fig. 2i–l. Fig. 2m–o represents the downslope angles -10° , -20° , -30° at 12 m s^{-1} ; and Fig. 2p–r shows -10° , -20° at 6 m s^{-1} and -10° at 3 m s^{-1} . The contours at 6 m s^{-1} cases are shown in Fig. S1 in Supplementary Appendix A (frames e–h).

At 12.5 m s^{-1} wind velocity, the fire front travels more quickly (than that of the lower wind velocity cases) and the plume leans (which leads to its attachment) towards the ground in all cases, as shown in Fig. 2a–d. At $+20^\circ$ and $+30^\circ$ slopes, the plume is more inclined towards the ground, as is evident for $+30^\circ$ where the plume can be seen attached nearly up to the end of the burnable plot. The same trend is generally observed with 6 m s^{-1} upslope cases as well (Fig. S1 in Supplementary Appendix A) where the plume can be seen inclined towards the ground; however, for the instances shown, the inclination distance (the distance covered by the plume when it is attached to the ground) is shorter compared with 12.5 m s^{-1} cases for the same upslope angle. However, inspecting the same data slightly later or earlier, the observation can be different on higher upslopes (for greater upslopes, the inclination distance may not at all time be shorter for 6 m s^{-1} compared with 12 m s^{-1}). The interaction between the plume and the terrain is captured clearly for $+30^\circ$ slope cases where the plume is leaning to nearly halfway along the burnable grass plot in most instances.

Frames (i–l) of Fig. 2 show that for 3 m s^{-1} wind velocity, the plume rises from the ground near the ignition line for 0° and $+10^\circ$ slopes, and for greater upslopes, the buoyant plume inclines towards the ground for a longer distance. However, compared with higher wind velocity cases, for the same slope angle, the plume rises earlier.

For downslopes, Fig. 2m–r, the plume rises from the ground earlier compared with upslope cases (at 12.5 m s^{-1} wind speed). As the downslope angle increases, the plume rises from the ground at shorter distances and the fire does not propagate, consistent with the fire isochrone progression shown in Part 1 of this paper, in *Progression of isochrones* section (Innocent et al. 2022). The fire extinguishes for downslopes at lower wind velocities (Fig. 2q–r), and hence steep downslopes (-30° at 6 m s^{-1} , -30° and -20° at 3 m s^{-1}) are not included in the plume and flame dynamics discussions.

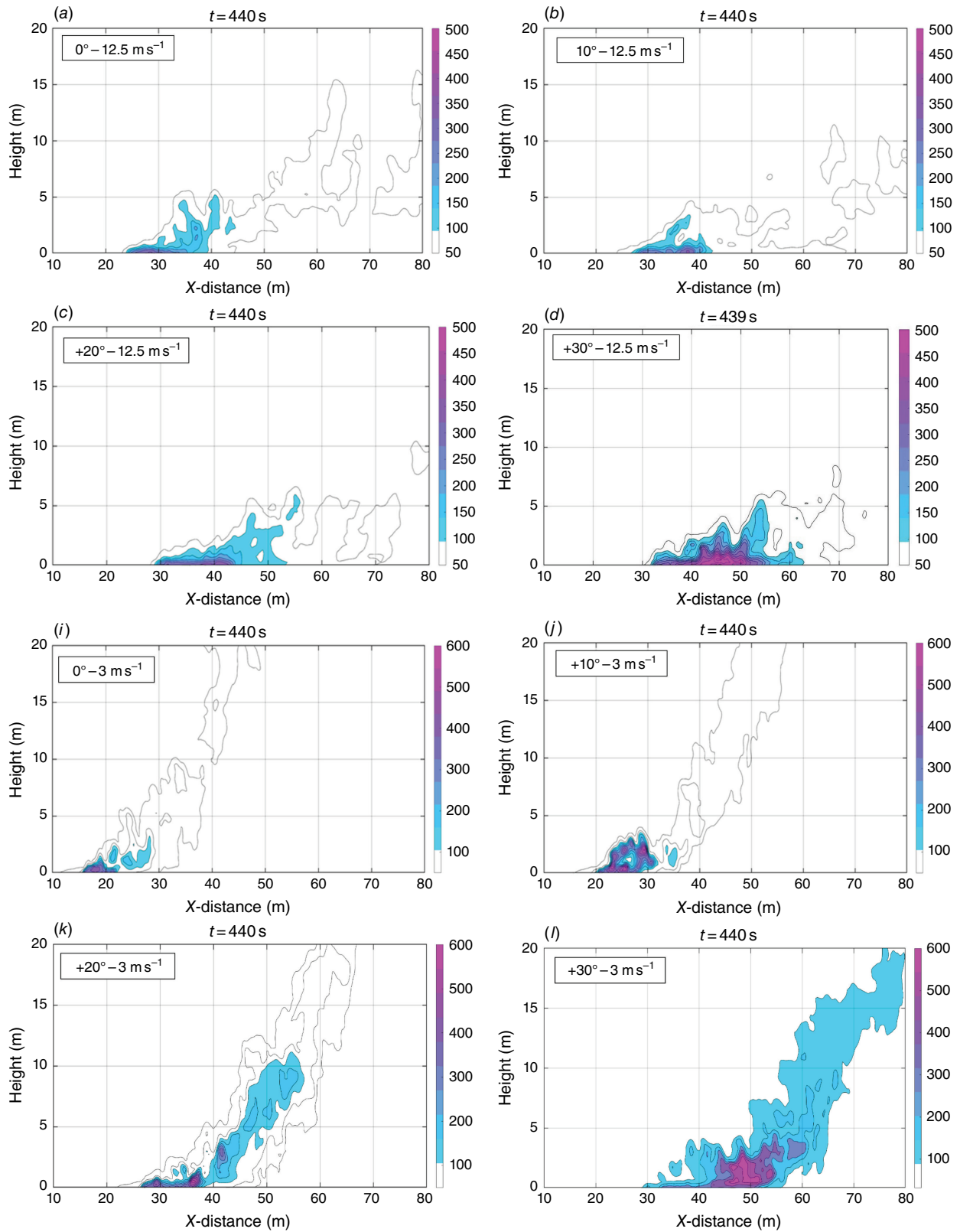


Fig. 2. Temperature contours (representing plumes) along the geometric centreline of the grass plot, at the same instant in time (30 s after ignition with ± 1 s variation): frames (a–d) 0° , $+10^\circ$, $+20^\circ$, $+30^\circ$ at 12 m s^{-1} ; frames (i–l) 0° , $+10^\circ$, $+20^\circ$, $+30^\circ$ 3 m s^{-1} ; frames (m–o) -10° , -20° , -30° at 12.5 m s^{-1} ; frames (p–r) -10° , -20° at 6 m s^{-1} and -10° at 3 m s^{-1} . Frames (e–h) 0° , $+10^\circ$, $+20^\circ$, $+30^\circ$ at 6 m s^{-1} are shown in Fig. S1 in Supplementry Appendix A.

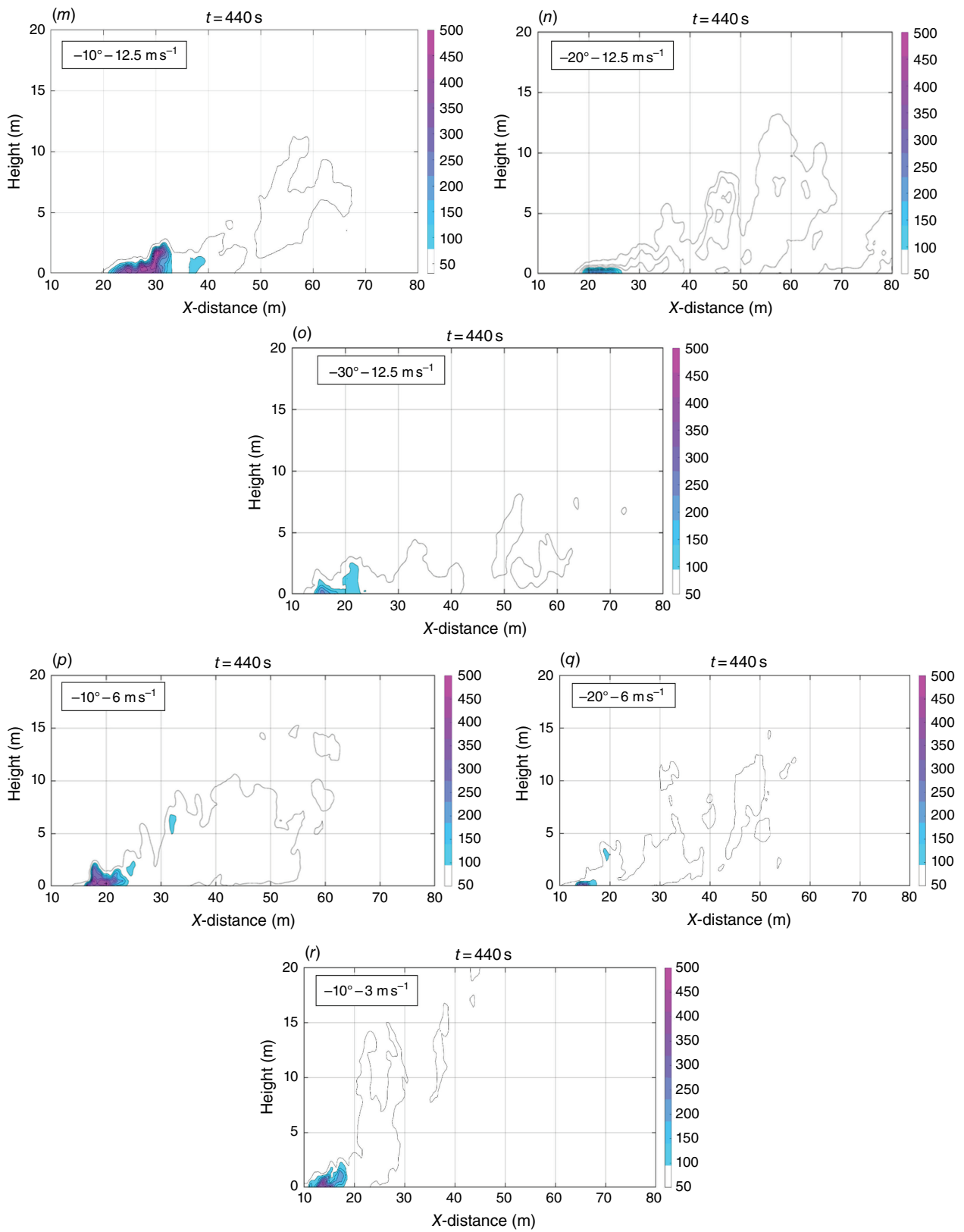


Fig. 2. (continued)

To compare the fires at a point where they have consumed a similar amount of fuel, we also present the fire plume contour at the same distance from the ignition line for all the cases. The plume contour at the same fire front position from the ignition line for 0° , $+10^\circ$, $+20^\circ$ and $+30^\circ$ are shown in Fig. S2 of Supplementary Appendix A for the three wind velocities. The plume contour shows a similar behaviour and interaction pattern as demonstrated by the contours plotted at the same instant in time (Fig. 2) for the respective wind velocity.

As the wind speed increases, leaning of the plume (which leads to its attachment to the ground) occurs at a much lower slope angle, as shown in Fig. 2a–d. Overall, these results show similarity to the observations of Dold and Zinoviev (2009) and Sharples (2017) that plume attachment occurs owing to an interaction between the slope of the terrain and the plume itself.

Defining and measuring where the flame is attached to the ground is difficult. Empirical measurements of flame attachment (for example, the experiments of Tang *et al.* 2017) are based on visual intensity thresholds in a prescribed region of interest. The detachment location shown in these frames of Fig. 3 is where the plume lifts off from the ground at that time frame. At detachment, the vertical velocity will be greater than the streamwise velocity (Burridge and Hunt 2017). It is then possible to study the behaviour of plume angle θ as a function of time, t , noting W and U are functions of time,

$$\theta(x, z, t) = \tan^{-1}\left(\frac{W}{U}\right), \quad (1)$$

where U and W are the streamwise and vertical components of the wind velocity at the Y centreline of the burnable grass plot, to estimate the detachment location. Specifically, we consider the mean of θ in the Z -direction, denoted

$$\bar{\theta}(x, t) = \theta(x, z, t)_z \quad (2)$$

in the neighbourhood of the flame. The detachment location, x_d , is then defined as the location of the first zero-crossing of $\bar{\theta}(x)$, that is, the first negative to positive crossing of average θ . The neighbourhood of the flame is taken as the rectangle extending from $Z = 0$ to five times the maximum Z -value of the flame contour, and from the minimum X -value of the pyrolysis region to $X =$ the location of the end of the burnable plot. Because we only consider the first (lowest X value) zero crossing, the maximum X -point in the neighbourhood is immaterial. The two points either side of the zero crossing are averaged to obtain x_d . As this process is repeated for all times, we obtain a time series of x_d . Note that each field discussed is at an instant in time and hence every quantity is then a function of time.

To understand the flame behaviour, it is useful to visualise the flame contours, temperature contours, detachment location and wind velocity vectors, taken through the centreline of the burnable grass plot, at various instants in time.

To visualise the flame contours, the output files obtained from the simulations were analysed using Matlab software. Streamwise and vertical components of wind velocity U and W , instantaneous heat release rate (HRR) and temperature data taken through the centreline of the burnable grass plot were analysed to obtain the contours and velocity quiver plots. The flame envelopes were determined from the minimum threshold temperature of 400 K to the maximum temperature of the flame. Coincidentally, the same 400 K threshold is used for flame envelopment as well as to denote the onset of pyrolysis of the surface fuel. Contours are plotted in Fig. 3 at five instants in time from the start of ignition for wind velocities of 12.5 and 3 m s^{-1} . The contours for 6 m s^{-1} cases are shown in Fig. S3, Supplementary Appendix A.

The plots show flame contour (red), with temperature contours (representing the plume) shaded in the background (yellow) along with flame detachment (or rising) locations (black dots) and wind vectors (white arrows) at slope angles $+30^\circ$, $+10^\circ$ and 0° . The wind velocity vectors are presented to visualise the flow pattern and demonstrate the dynamic behaviour as the fire progresses. Such dynamic behaviour is the result of dynamic pressure differences between zones upstream and downstream of the flame, consistent with Eftekharian *et al.* (2019, 2020). The vectors show instantaneous flow direction and thus a picture of the turbulence at a particular instant. In order to understand entrainment trends, one would need to build an ensemble average of the wind as the fire moves. This has been attempted by Sutherland *et al.* (2022). However, it is beyond the scope of the current manuscript.

Fig. 3a–o represents $+30^\circ$, $+10^\circ$ and 0° at wind velocity 12.5 m s^{-1} . For the highest slope angle, $+30^\circ$, at the initial instant of time, the near-flame behaviour is vertical, and the flame-perturbed velocity vector is upwardly inclined. However, at (x, z) locations far downstream from the ignition line, the plume (represented by the temperature contour) is horizontal with little vertical perturbation. The flame-perturbed velocity vector inclination is closer to the surface. The flame dynamics indicates that the flame appears to rise up; however, the plume is leaning or attached to the ground (see Fig 3c–e) as similarly observed in the plume contour in Fig. 2d, indicating that the flame does not necessarily follow the plume behaviour. At 1 or 2 m above the ground where the wind velocity is lower, the flame behaviour appears to be buoyancy-driven (or closer to buoyancy-driven mode), whereas at higher Z , the velocity vector is horizontal, consistent with a wind-driven fire. As the fire moves forward, it becomes more buoyancy-dominated and the flame becomes deeper (Fig 3c, d) and finally, the flame shrinks as the fuel is depleted. Cases with slope angles $+10^\circ$ and 0° follow a similar pattern: buoyancy-dominated flame near the ground, tending towards wind-dominated fire for a very short time and then transitioning to buoyancy-dominated as the fire

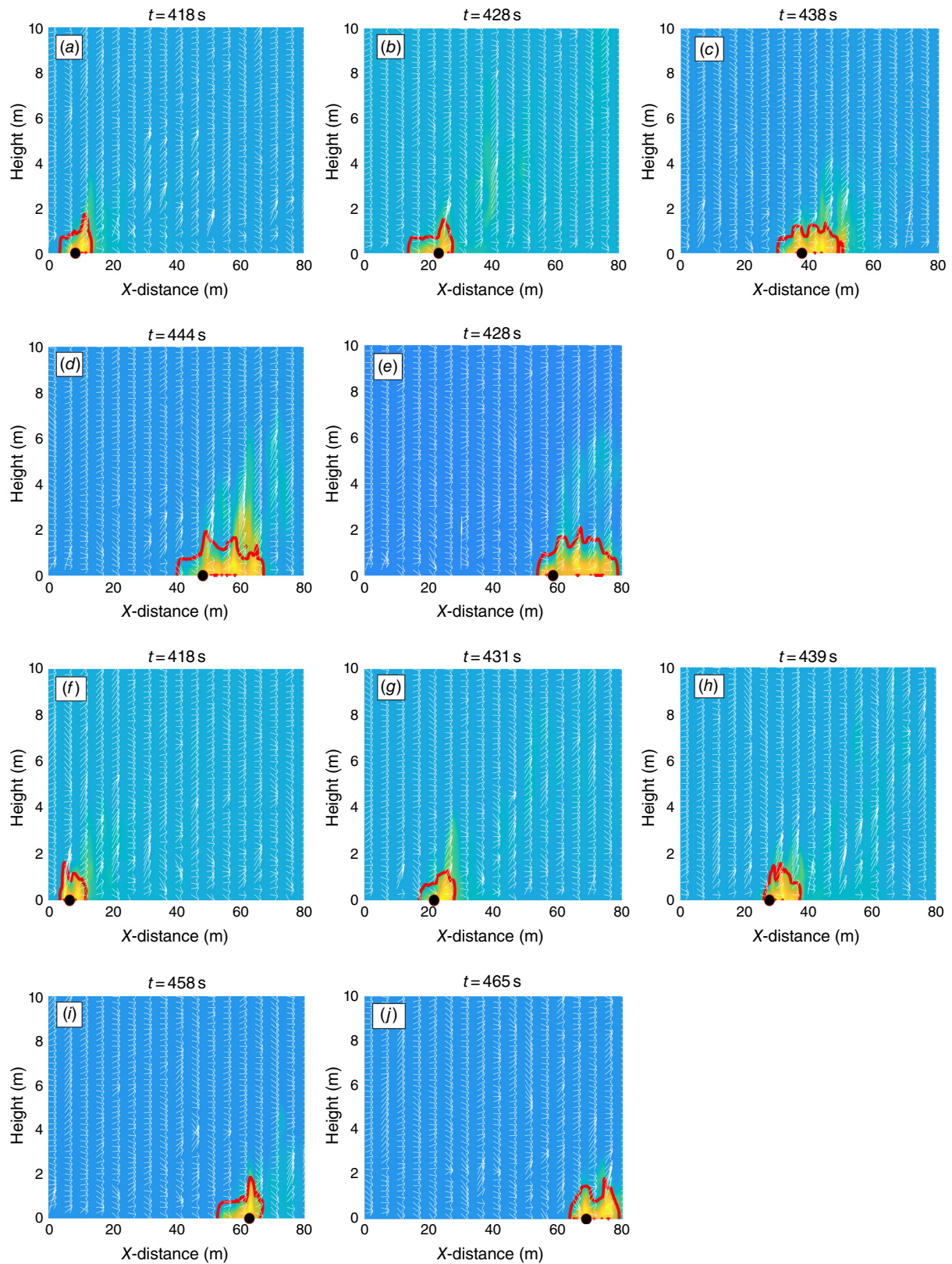


Fig. 3. Flame contour (red) with temperature contour (representing plume) shaded (yellow) in the background along with detachment locations (black dot; this point may occur in the flame or in the plume) and wind vector plots (white arrows) at various instants in time for wind velocities of 12.5 and 3 m s^{-1} . Frames (a–c): $+30^\circ$, $+10^\circ$ and 0° at 12.5 m s^{-1} , and (d–j): $+30^\circ$, $+10^\circ$ and 0° at 3 m s^{-1} .

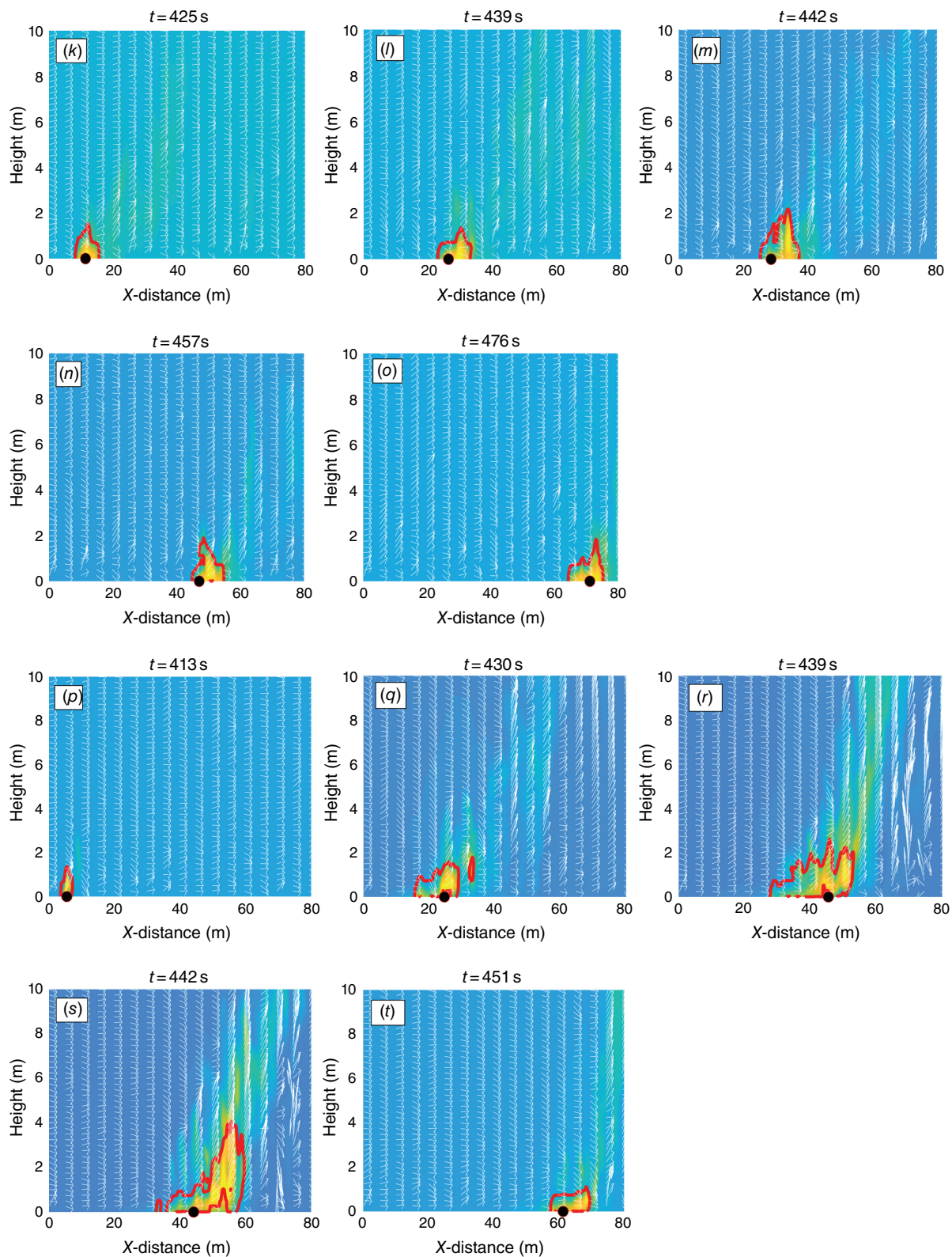


Fig. 3. (continued)

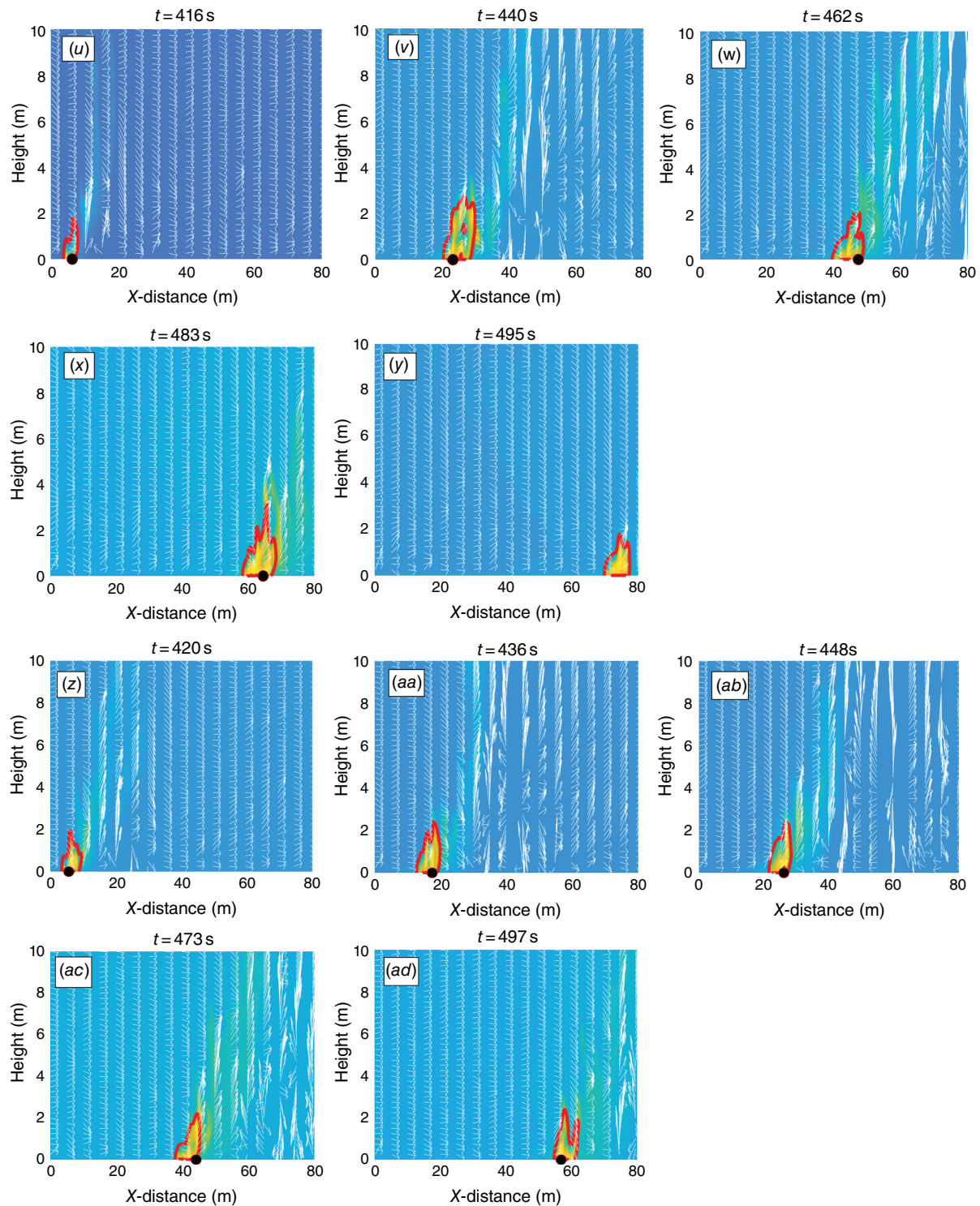


Fig. 3. (continued)

progresses. The flame becomes deeper as the slope angle increases. For no slope, generally, the flame remains vertical and pointing upwards compared with higher slope angles, as evident in Fig 3l–n. When the fire runs uphill, the flame length is found to be higher at the instant the flame is

attached to the terrain, which is consistent with the study of Dold and Zinoviev (2009).

The +30°, +10° and 0° plots at wind velocity 6 m s⁻¹ are presented in Fig. S3ae–as, Supplementary Appendix A. The plots generally reflect the same trend as for 12.5 m s⁻¹

cases. For the no-slope cases, a rising flame is observed throughout (Fig. S3ap–ar); however, as the slope angle increases, some intermittent attachment occurs, resulting in subsequent flaring up of the flame. The flame is more vertical for the 0° case compared with the +30° case. As the slope angle increases, the flame becomes deeper as the fire moves forward. For higher slopes, the plumes tend to be rising more compared with the cases at the higher wind velocity 12.5 m s⁻¹ and appear to be more within the buoyancy-dominated regime. The +30°, +10° and 0° plots at driving wind velocity 3 m s⁻¹ are presented in Fig. 3p–ad. Compared with 12.5 and 6 m s⁻¹, the plumes emanating from the grass plot rise up (and are vertical), as similarly observed in Fig. 2i–l. The fire establishes itself and then becomes inclined to the ground, which leads to rapid intensification and a buoyancy-dominated fire (Fig. 3r, s). The rising of the flame is more evident in the 0° case (frames aa–ac). For lower slope angles, the flame is more vertical; however, the flame becomes deeper for the highest slope angle of +30°. This agrees with Mendes-Lopes *et al.* (2003), who in their low-velocity experimental studies observed that the flame tended to be vertical owing to buoyancy forces.

Byram's convective number (N_c), a dimensionless parameter, is used to quantify the mode of fire propagation as wind-driven or buoyancy-driven fire mode (Morvan and Frangieh 2018; Mell *et al.* 2018). N_c uses the wind velocity at 10 m (U_{10}) as the relevant velocity scale. However, the results shown in Fig. 3 demonstrate that the flame behaviour can be different from the overall plume behaviour and that N_c based on U_{10} may capture the plume behaviour but not the flame behaviour.

Mode of fire propagation

To understand the modes of heat transfer and fire behaviour, we calculated Byram's convective number N_c . The N_c , which is the ratio between buoyancy and inertia forces (Morvan and Frangieh 2018) is given by Eqn 3:

$$N_c = \frac{2gQ}{(U_{10} - \text{RoS})^3 \rho c_p T_a} \quad (3)$$

where U_{10} is the open wind velocity at a height of 10 m (in a zone not affected by the fire), RoS is the rate of spread (m s⁻¹), Q is the fireline intensity (kW m⁻¹) of the fire, T_a is the ambient temperature, taken here as 305 K, $g = 9.8 \text{ m s}^{-2}$ is the acceleration due to gravity, ρ (kg m⁻³) is the gas density (1.2 kg m⁻³) and $c_p = 1.0 \text{ kJ kg}^{-1} \text{ K}^{-1}$ the specific heat of air. If $N_c > 10$, the fire is buoyancy-driven, and if $N_c < 2$, the fire is wind-driven. At intermediate N_c values, the fire is neither buoyancy-driven nor wind-driven. However, as N_c is dimensionless, this study exercises the discretion to choose the velocity at any relevant height to analyse the fire behaviour.

For the simulations presented here, the RoS and Q values are taken from the measurements shown in *RoS Calculations*

and *Fire Intensity* sections of Innocent *et al.* (2022), respectively. Both RoS values – the quasi-steady RoS measured from the slope of the fire front location (by applying a linear fit to the fire front location in time) and the averaged dynamic RoS (obtained by differentiating the fire front location data) – are used to compute different N_c values. Although there are differences between the values computed using the two measurements of RoS, none of the differences is significant enough to change the classification of the mode of fire propagation. The HRR (kW) values obtained at various instants in time are divided by the measured fire front length (m) to obtain fire intensity (Q) and determine the quasi-steady Q value (kW m⁻¹) of the respective simulation.

The N_c values derived from Eqn 3 using both the quasi-steady RoS and dynamic average RoS values are shown in Fig. 4a. Following Morvan and Frangieh (2018), the N_c values in Fig. 4a are based on U_{10} wind velocities of 12.5, 6 and 3 m s⁻¹, referred to as N_{c10} in the discussion.

For simulations with 12.5 m s⁻¹, N_{c10} is observed to be lower than 2 and hence within the wind-driven regime for all slope angles. With wind speed 6 m s⁻¹, $N_{c10} < 2$ for slope angles -30° to +10°, indicating a wind-driven fire. However, for greater upslopes (+20° and +30°), N_{c10} lies between $2 < N_{c10} < 10$, which indicates that these fires are in the intermediate regime. At the lowest wind speed 3 m s⁻¹, the upslope cases 0° to +30° can be classified as buoyancy-driven given the large N_{c10} (although for the 0° case, N_{c10} is close to the threshold value of 10). The -10° case is in the intermediate regime. For all no-slope cases, the N_{c10} values were found to be consistent with the observation of Sutherland *et al.* (2020).

Unusually, a very high Byram number value ($N_{c10} > 500$) was observed for wind velocity 3 m s⁻¹ with +30° slope but the instantaneous temperature contour (Fig. 2l) shows that the plume is leaning to the burnable grass plot for a considerable distance (almost half of the plot). However, the plume eventually rises up approximately 55 m downstream and becomes more vertical. In this case, the flame is wind-driven and initially, the flame shape appears similar to the 12.5 m s⁻¹ wind-dominated cases. The flame eventually erupts (transitions to a rising plume) and becomes more like the buoyancy-dominated flames towards the end of the burnable plot.

Because the Byram number is a comparison of buoyancy forces originating at the surface with the shearing forces driven by the horizontal wind at 10 m, it is possible that the near-surface flame dynamics could be misclassified.

To understand the near-surface flame and wind field behaviour, wind velocity at 2 m (U_2) was used in the N_c calculations in place of U_{10} . U_2 is traditionally considered as the mid-flame wind velocity. Mean velocity profiles were extracted from the centreline U -velocity slices and U_2 values were found to be 8.7, 4.4 and 2.2 m s⁻¹ for corresponding U_{10} values of 12.5, 6 and 3 m s⁻¹.

The N_c values derived using U_2 , referred to as N_{c2} in the discussion, are presented in Fig. 4b. For the highest wind

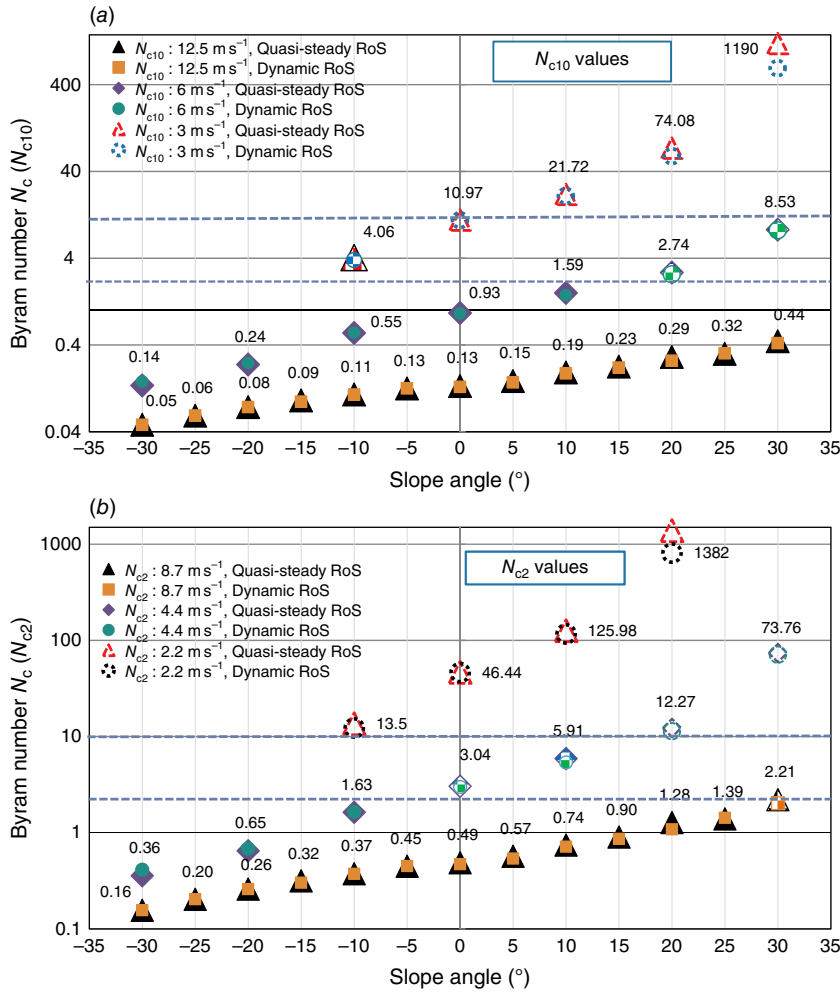


Fig. 4. Byram's convective number N_c vs slope angle, derived using both quasi-steady RoS and dynamic average RoS: (a) N_{c10} based on U_{10} of 12.5, 6 and 3 m s⁻¹; (b) N_{c2} based on U_2 of 8.7, 4.4 and 2.2 m s⁻¹. Plots are in logarithmic scale (y-axis). The N_c values using quasi-steady RoS are indicated in the plots. Wind-driven fire propagation is shown as solid symbols, buoyancy-driven is shown as hollow symbols and the intermediate regime is shown as pattern-filled symbols.

velocity, $U_2 = 8.7 \text{ m s}^{-1}$, the fire is within the wind-driven regime $N_{c2} < 2$; however, for higher upslope cases, the values are notably closer to the threshold value 2, with +30° slope falling in the intermediate regime. The near-surface flame appears to be detached or rising up and the fire may not be entirely wind-driven (as observed with N_{c10} values using $U_{10} = 12.5 \text{ m s}^{-1}$ in Fig. 4a), though the plume went over to the wind-driven regime. This agrees with the flame and near-surface flame rising detailed in *Plume and Flame dynamics* section, Fig. 3a–o.

With $U_2 = 4.4 \text{ m s}^{-1}$, $N_{c2} < 2$ for slope angles -30° to -10°, indicating a wind-driven fire, as observed in Fig. 4b. However, for 0° and +10°, N_{c2} values are higher and lie between $2 < N_{c2} < 10$, indicating an intermediate fire regime, whereas 0° and +10° slopes are in the wind-driven regime with $U_{10} = 6 \text{ m s}^{-1}$, as shown in Fig. 4a. For greater upslopes (+20° and +30°), $N_{c2} > 10$, classifying these as buoyancy-driven fire regimes, a clear shift from the intermediate regime with U_{10} (Fig. 4a) to a buoyancy-driven regime with U_2 . For larger upslopes, the plumes at lower wind velocities are more likely to be rising over a longer distance than the higher wind velocity cases and

appear to be more in the plume-dominated regime, in line with the flame contour plots (Fig. 3a–e, p–t).

At the lowest wind speed, $U_2 = 2.2 \text{ m s}^{-1}$, all upslope cases can be clearly classified as buoyancy-driven, given the large N_{c2} values, which agrees with the N_{c10} analysis using U_{10} (Fig. 4a) except for downslope 10°, which is in the intermediate regime using U_{10} but moves into the buoyancy-dominated region using U_2 . The eruption in Fig. 3r, s could not be explained by using U_2 in place of U_{10} in the Byram number calculation.

The mode of fire propagation for all slope cases at the three wind velocities based on N_c calculations (N_{c10} and N_{c2}) is summarised in Table 2.

Flame length

The flame length was computed from instantaneous centreline HRR data. The geometric centreline HRR data were analysed at every time step and 99% of the maximum observed HRR value was used as the threshold value to create a binary image. The data inside the threshold contour take the value one and the data outside take the value zero.

Table 2. Summary: mode of fire propagation based on N_c calculation.

Slope angle	N_{c10} (based on U_{10})			N_{c2} (based on U_2)		
	12.5 m s^{-1}	6 m s^{-1}	3 m s^{-1}	8.7 m s^{-1}	4.4 m s^{-1}	2.2 m s^{-1}
-30°	Wind-driven			Wind-driven		
-25°	Wind-driven			Wind-driven		
-20°	Wind-driven	Wind-driven		Wind-driven	Wind-driven	
-15°	Wind-driven			Wind-driven		
-10°	Wind-driven	Wind-driven	Intermediate	Wind-driven	Wind-driven	Buoyancy-driven
-5°	Wind-driven			Wind-driven		
0°	Wind-driven	Wind-driven	Buoyancy-driven	Wind-driven	Intermediate	Buoyancy-driven
$+5^\circ$	Wind-driven			Wind-driven		
$+10^\circ$	Wind-driven	Wind-driven	Buoyancy-driven	Wind-driven	Intermediate	Buoyancy-driven
$+15^\circ$	Wind-driven			Wind-driven		
$+20^\circ$	Wind-driven	Intermediate	Buoyancy-driven	Wind-driven	Buoyancy-driven	Buoyancy-driven
$+25^\circ$	Wind-driven			Wind-driven		
$+30^\circ$	Wind-driven	Intermediate	Buoyancy-driven	Intermediate	Buoyancy-driven	Buoyancy-driven

Following Cobian-Iñiguez *et al.* (2019), an ellipse was fitted to the binary image at every time level using Matlab (Davis and Sigmon 2005) function *regionprops*. The ellipse was constrained so that the second moment of the ellipse was equal to the second moment of the non-zero region of the image. The flame length was computed from the major axis of the fitted ellipse, which represents the distance from the centre of the flame base to the tip of the flame. The flame length values fluctuate and show irregularity due to the dynamic nature of fire propagation.

Fig. 5a shows flame length vs time plotted for upslopes and downslopes at wind velocity 12.5 m s^{-1} . The flame lengths for 6 and 3 m s^{-1} can be found in Fig. S4b, c, Supplementary Appendix A, respectively, and in Fig. S4d, e, Supplementary Appendix A, the results from the longer burnable grass plot simulations for greater upslopes (repeated to ensure a quasi-steady state) at wind velocities 12.5 and 6 m s^{-1} are presented, respectively.

In Fig. 5a, upslope cases show the greatest flame length at $+30^\circ$ slope and the flame length decreases as the slope angle decreases. The peak flame length value for an upslope angle was found to be approximately 30% higher than the flame length of the next lower angle (by 10°); however, the difference narrows as the wind velocity decreases. This observation is consistent with the plume contour views of Fig. 2a–l: when the upslope angle increases, the plume inclines towards the ground and is more prone to plume attachment. The flame lengths are much higher for upslopes than downslopes. For downslopes, the flame length is greatest at -10° and the length decreases with increase in downslope angle. The difference in flame lengths is lower than that observed for upslopes. Comparing among the three velocity cases, for corresponding slopes (Fig. S4,

Supplementary Appendix A), the flame length is generally lower for the lower-velocity cases. This indicates that with the higher wind velocity, convection plays an increased role in fire propagation.

The flame length values extracted from the quasi-steady region are plotted in Fig. 5b for the three wind velocities. At lower wind velocities and with steep downslopes, the fire front does not propagate down the slope. Therefore, -30° at 6 m s^{-1} , -30° and -20° at 3 m s^{-1} are not included in the flame length plots.

Alexander and Cruz (2012, 2021) examined the underlying assumptions and limitations associated with various empirical correlations between fireline intensity and flame length. They found that fire behaviour characteristics are strongly influenced by the fuel structure and environmental conditions and there are bounds or limits associated with these empirical relationships. Alexander and Cruz (2012, 2021) presented a list of power-law correlations to facilitate estimation of the flame length as a function of the fire line intensity. Similarly, Barboni *et al.* (2012) presented another list of correlations. We attempted to find which of these correlations best fitted our numerical data and found that the best results were obtained with the correlations derived by Anderson *et al.* (1966), which is listed among the correlations presented in Alexander and Cruz (2012, 2021). They proposed flame length as a function of fire line intensity, as shown in Eqn 4, derived from field experiments conducted using a surface fuel of lodgepole pine slash:

$$L = 0.074Q^{0.651}, \quad (4)$$

where L is the flame length in metres. For the simulations presented here, the Q values (kW m^{-1}) were taken from the

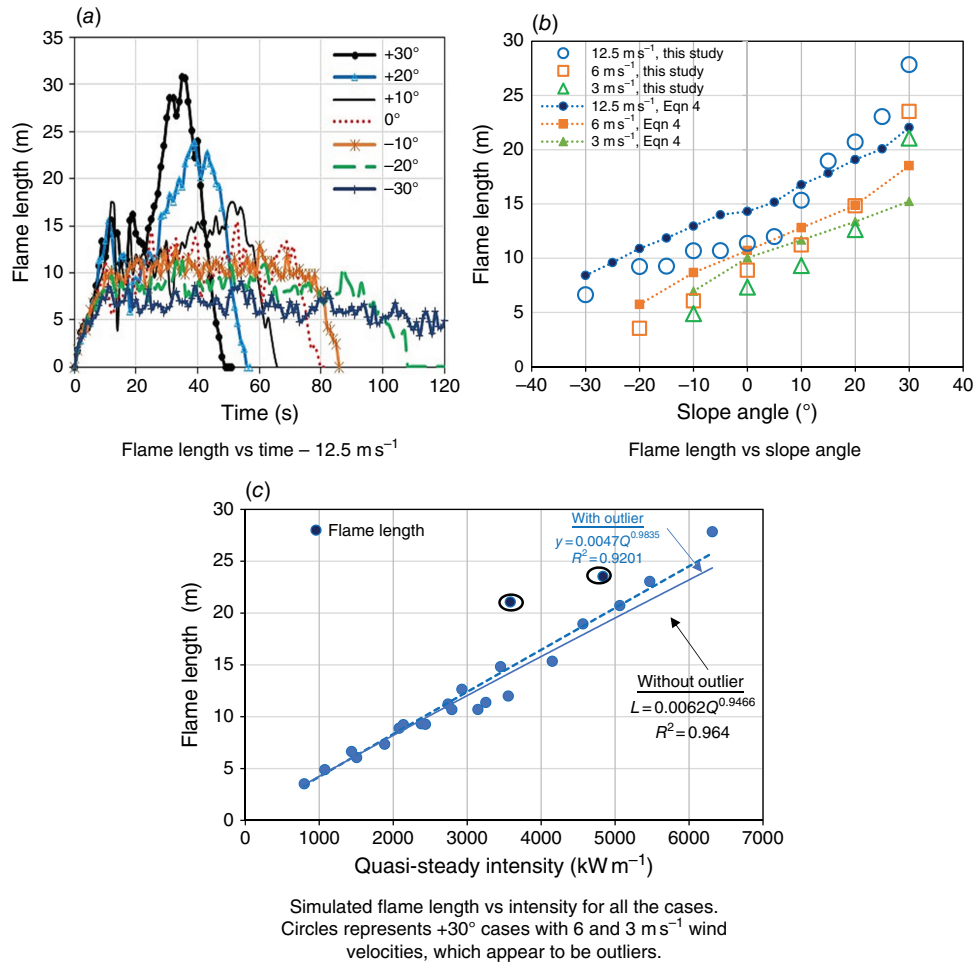


Fig. 5. (a) Flame length vs time at wind velocity 12.5 m s⁻¹; (b) quasi-steady flame length vs slope angles from this study along with empirically derived values, at 12.5, 6 and 3 m s⁻¹; (c) simulated quasi-steady flame length vs simulated quasi-steady intensity showing existence of a power-law relationship (ovals represent +30° cases with 6 and 3 m s⁻¹ wind velocities which appear to be outliers).

preceding part of this study, *Heat Release Rate and Fire Intensity* section (Innocent et al. 2022). The values of L calculated using Eqn 4 are presented in Fig. 5b, along with the quasi-steady L values obtained from this study (Q values corresponding to the respective slope angles and wind velocities are used in Eqn 4). The L values predicted by Eqn 4 are nominally higher than the values obtained from this study for slope angles up to +10°. For larger upslopes, Eqn 4 predicts lower values than the simulation results (especially for 12.5 m s⁻¹ cases). Presenting all the simulated L values against the simulated Q values in Fig. 5c, a power-law relationship, Eqn 5, was found to exist between the flame length and intensity, in broad agreement with the correlations in the list of empirical models presented in Alexander and Cruz (2012, 2021) and Barboni et al. (2012):

$$L = 0.0062Q^{0.9466} \quad (5)$$

The +30° cases with 6 and 3 m s⁻¹ wind velocities appear to be outliers (shown with ovals in Fig. 5c) and were omitted from the linear regression fit.

Flame height (defined as the vertical distance from the base of the leading edge of the flame to the flame tip) could not be reliably determined from the simulation data. An attempt was made using a method similar to the one used to compute flame length (Cobian-Iñiguez et al. 2019), and the flame height was computed analogously from the maximum height of the fitted ellipse. Using this method, we found that the flame height does not generally vary with slope and is within the range of 1–1.8 m. However, there may be limitations in the ellipse-fitting approach used here.

Heat fluxes

To understand the role of radiative and convective heat transfer on sloped terrain, contour plots of heat fluxes

were analysed and are presented in Fig. 6. The modelling (and correlations) of the net convective and radiative heat transfer to the vegetation in the Large Eddy Simulation (LES) approach implemented in WFDS can be found in Mell *et al.* (2009), McGrattan *et al.* (2015) and Perez-Ramirez *et al.* (2017).

The convective and radiative heat flux boundary data obtained from the simulations were analysed using Matlab to extract the contours. The averaged heat flux data at every cell in time impinging over the unburnt fuel were analysed. The heat flux data were derived based on the trailing edge (or pyrolysis rear) of the pyrolysis region, as the fire front

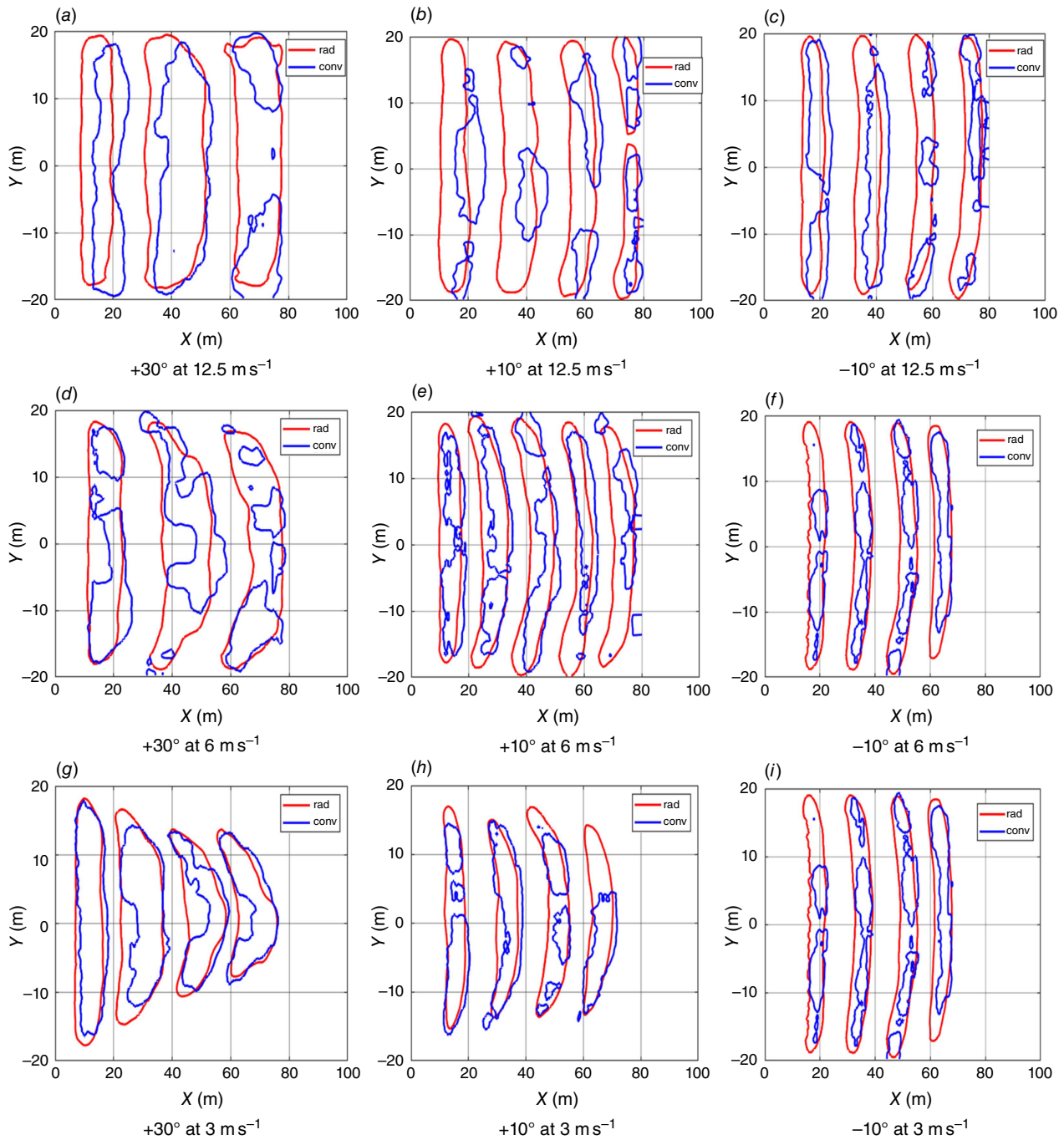


Fig. 6. Instantaneous heat flux contours taken at different times as the fire front moves through the grass plot for slope angles $+30^\circ$, $+10^\circ$ and -10° at: (a–c) 12.5 m s^{-1} ; (d–f) 6 m s^{-1} ; and (g–i) 3 m s^{-1} ; ‘rad’ and ‘conv’ represent radiative and convective heat fluxes, respectively. See the discussion for an explanation of these heat flux contours.

moved from left to right through the burnable grass plot. As there is no physically meaningful threshold for the heat fluxes, the data were normalised to range from 0 to 1 and the 0.5 value contour was plotted. That is, 50% of the heat transfer occurs inside the contour. The instantaneous heat flux contours were taken at different times as the fire front moved through the grass plot for +30°, +10° and -10° slopes at the three wind velocities.

At 12.5 m s⁻¹, the convective heat flux (blue lines) tends to lie ahead of the radiative heat flux (red lines) for all three slopes. The convective heat flux is the leading heat transfer mechanism for 12.5 m s⁻¹ cases, which are predominantly wind-driven fire propagation as demonstrated in the Byram number analysis. The trend of convective heat flux leading the radiative heat flux also occurs at 6 m s⁻¹ with +30° and +10° slopes, whereas it remains spatially overlapping or lagging at some instances with the -10° slope. However, at a lower wind velocity of 3 m s⁻¹, the radiative heat flux contours mostly overlap the convective heat flux contours.

The leading or lagging of the fire front by the convective heat flux does not necessarily mean that the total heat flux is dominated by the convective heat flux. Rather, these contours provide information about where the heat transfer occurs.

The results presented show that the convective heat fluxes are more relevant in wind-driven fires and at greater slopes compared with buoyancy-driven fires and for lower slopes; these results are consistent with the studies of Sánchez-Monroy et al. (2019) and Dupuy and Maréchal (2011).

The total radiative and convective heat fluxes on the plot ahead of the fire front at 12.5 m s⁻¹ are presented in Fig. 7a, c, respectively. The results from repeated simulations with the longer 120-m grass plot (to ensure quasi-steady state) are presented in Fig. S5, Supplementary Appendix A. The heat fluxes for 6 and 3 m s⁻¹ are shown in Fig. S6a-d, Supplementary Appendix A. To obtain these data, the boundary heat flux data at every time step were multiplied by a filter that discriminates between burnt and unburnt fuel. The heat flux to the unburnt surface was summed to get the total boundary heat flux value (both radiative and convective) at that instant of time. For all three wind velocities, with increasing slope angle, the heat fluxes reach their maximum values earlier, as the fire front travels much more quickly on upslopes. The heat flux increases as the fire front progresses from the ignition line, then reaches a quasi-steady state and finally decreases. The total heat fluxes increase with slope angle and wind velocity.

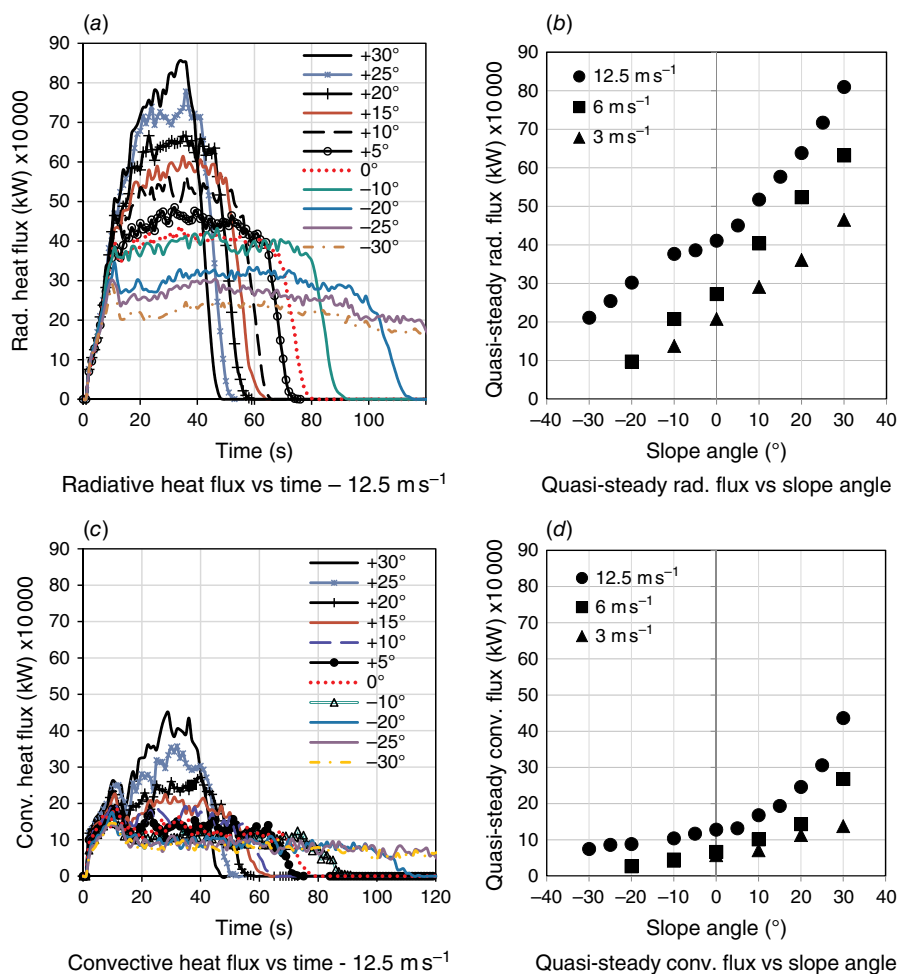


Fig. 7. Heat fluxes as a function of time: (a) radiative heat flux vs time at velocity 12.5 m s⁻¹; (b) quasi-steady radiative heat flux vs slope angles at velocities 12.5, 6 and 3 m s⁻¹; (c) convective heat flux vs time at 12.5 m s⁻¹; (d) quasi-steady convective heat flux vs slope angles at velocities 12.5, 6 and 3 m s⁻¹. (Radiative (Rad.) and convective (Conv.) heat fluxes for 6 and 3 m s⁻¹ are shown in Fig. S6a-d, Supplementary Appendix A.)

However, the opposite scenario is found with the downslopes. At lower wind velocities 6 and 3 m s^{-1} , for steep downslopes, the fires fail to sustain themselves (Fig. S6a–d, Supplementary Appendix A) and both the convective and radiative heat flux values are much lower (-30° at 6 m s^{-1} , -30° and -20° at 3 m s^{-1}).

The radiative and convective heat flux values extracted from the quasi-steady region are plotted against slope angles in Fig. 7b, d for the three wind velocities. For a given slope angle, the radiative heat flux is higher than the convective heat flux for all three wind velocities. Comparing among the velocities, as the driving wind velocity increases, both radiative and convective heat flux values increase. For 12.5 m s^{-1} , the radiative heat flux value for the greater upslope ($+30^\circ$) is approximately 95% higher than that for no-slope, and for greater downslope (-30°) is approximately 94% lower than no-slope. The convective heat flux value for the larger upslope is approximately 200% higher than no-slope and that for the larger downslope (-30°) is approximately 72% lower than no-slope. For lower wind velocities 6 and 3 m s^{-1} , the convective heat flux values are closer for slope angles -30° to $+10^\circ$, indicating that the wind velocity has less effect on the convective heat flux for downslopes compared with its effect on radiative heat flux.

Conclusions

In this study, the interactions of wind and slope on fire propagation and dynamics were explored with physics-based simulations. We considered a particular surface fuel type (with specific thermo-physical properties) with fixed fuel bed conditions (fuel load, bulk density and fuel height). Within the simulations conducted, it was found that with increasing upslope angle and wind velocities, the plume inclines more towards the ground whereas on downslopes, the plume rises from the ground earlier. Bearing in mind that our simulations are at a much smaller scale than a real wildfire scenario, we found that with larger upslopes, the eruptive growth of fires may lead to flame attachment, which can result in firefighter casualties (Lahaye *et al.* 2018). Our results indicate that such attachment can occur in higher upslope cases ($> +20^\circ$ slopes). However, our highly idealised simulations are at a small scale and caution must be applied in extrapolating these results. As wind speed increases, the plume attachment occurs at a much lower slope angle owing to an interaction between the slope of the terrain and the plume itself. For higher wind velocities, the flame and near-flame appear to be rising, even though the plume is attached. Overall, we found similarities with the results of Dold and Zinoviev (2009) and Sharples (2017).

Considering the behaviour of the plume at higher altitudes, at $Z = 10 \text{ m}$, it appears to be wind-driven in agreement with the Byram number analysis. For higher wind velocities (12.5 and 6 m s^{-1}), the flame is buoyancy-dominated near

the ground, tends towards wind-dominated for a very short time intermittently and then transitions to buoyancy-dominated regime as the fire progresses. At lower wind velocity (3 m s^{-1}), the plume rises up, the fire establishes itself and the flame then becomes attached, which leads to rapid intensification and a buoyancy-dominated fire. The flame is more vertical at lower slope angles and becomes deeper as the slope angle increases. To understand the near-flame wind field behaviour, wind velocity at 2 m (U_2) was used in the Byram number calculation in place of U_{10} . Within the simulations conducted in this study, the flame behaviour can be different from the overall plume behaviour and the Byram number based on U_{10} captures the plume behaviour, not the flame behaviour.

When the fire ran uphill, the flame length was found to be higher with the flame attached to the ground. Flame length at a given slope angle increased with the driving wind velocity. For all three wind velocities, the flame lengths obtained from this study were found to reasonably agree with the values predicted by the empirical model proposed by Anderson *et al.* (1966). Additionally, within the simulated flame lengths and intensity, a power-law correlation between the flame length and fireline intensity exists.

The contours of heat fluxes show that the convective heat fluxes are more relevant for wind-driven fire propagation and on larger upslopes. Both the total radiative and the total convective heat flux values increased with wind velocity. Similar observations were reported by Mendes-Lopes *et al.* (2003), Dold and Zinoviev (2009), Dupuy and Maréchal (2011), Sharples (2017) and Sánchez-Monroy *et al.* (2019). For a given slope angle, the total radiative heat flux values were higher than convective heat flux values for all three driving wind velocities. However, the difference between the fluxes decreased as the wind velocity decreased and both fluxes were equally significant at lower driving wind velocity compared with higher wind velocities. Sánchez-Monroy *et al.* (2019) reported that for no-wind conditions on slopes above 30° , convective heat flux was larger and a tendency towards that was observed in our study.

Supplementary material

Supplementary material is available [online](#).

References

- Alexander ME, Cruz MG (2012) Interdependencies between flame length and fireline intensity in predicting crown fire initiation and crown scorch height. *International Journal of Wildland Fire* **21**, 95–113. doi:10.1071/WF11001
- Alexander ME, Cruz MG (2021) *Corrigendum to: Interdependencies between flame length and fireline intensity in predicting crown fire initiation and crown scorch height. International Journal of Wildland Fire* **30**, 70. doi:10.1071/WF11001_C1
- Anderson H, Brackebusch AP, Mutch RW, Rothermel RC (1966) Mechanisms of fire spread Research Progress Report No. 2. Research Paper INT- 28. (US Forest Service)

- Apte VB, Bilger RW, Green AR, Quintiere JG (1991) Wind-aided turbulent flame spread and burning over large-scale horizontal PMMA surfaces. *Combustion and Flame* **85**, 169–184. doi:10.1016/0010-2180(91)90185-E
- Barboni T, Morandini F, Rossi L, Molinier T, Santoni P-A (2012) Relationship between flame length and fireline intensity obtained by calorimetry at laboratory scale. *Combustion Science and Technology* **184**, 186–204. doi:10.1080/00102202.2011.625373
- Burridge HC, Hunt GR (2017) From free jets to clinging wall jets: The influence of a horizontal boundary on a horizontally forced buoyant jet. *Physical Review Fluids* **2**, 023501. doi:10.1103/PhysRevFluids.2.023501
- Chen TBY, Yuen ACY, Wang C, Yeoh GH, Timchenko V, Cheung SCP, Chan QN, Yang W (2018) Predicting the fire spread rate of a sloped pine needle board utilizing pyrolysis modelling with detailed gas-phase combustion. *International Journal of Heat and Mass Transfer* **125**, 310–322. doi:10.1016/j.ijheatmasstransfer.2018.04.093
- Cobian-Iñiguez J, Aminfar A, Weise DR, Princevac M (2019) On the use of semi-empirical flame models for spreading chaparral crown fire. *Frontiers in Mechanical Engineering* **5**, 50. doi:10.3389/fmech.2019.00050
- Davis T, Sigmon K (2005) ‘MATLAB Premier’, 7th edn. (Chapman & Hall/CRC)
- Dold JW, Zinoviev A (2009) Fire eruption through intensity and spread rate interaction mediated by flow attachment. *Combustion Theory and Modelling* **13**, 763–793. doi:10.1080/13647830902977570
- Dupuy J-L, Maréchal J (2011) Slope effect on laboratory fire spread: contribution of radiation and convection to fuel bed preheating. *International Journal of Wildland Fire* **20**, 289–307. doi:10.1071/WF09076
- Eftekharian E, Ghodrat M, He Y, Ong RH, Kwok KCS, Zhao M (2019) Numerical analysis of wind velocity effects on fire-wind enhancement. *International Journal of Heat and Fluid Flow* **80**, 108471. doi:10.1016/j.ijheatfluidflow.2019.108471
- Eftekharian E, Ghodrat M, He Y, Ong RH, Kwok KCS, Zhao M (2020) Correlations for fire-wind enhancement flow characteristics based on LES simulations. *International Journal of Heat and Fluid Flow* **82**, 108558. doi:10.1016/j.ijheatfluidflow.2020.108558
- Finney MA, Cohen JD, Forthofer JM, McAllister SS, Gollner MJ, Gorham DJ, Saito K, Akafuah NK, Adam BA, English JD (2015) Role of buoyant flame dynamics in wildfire spread. *Proceedings of the National Academy of Sciences* **112**, 9833–9838. doi:10.1073/pnas.1504498112
- Innocent J, Sutherland D, Khan N, Moinuddin K (2022) Physics-based simulations of grassfire propagation on sloped terrain at field-scale: motivations, model reliability and rate of spread. *International Journal of Wildland Fire*. doi:10.1071/WF22124
- Lahaye S, Sharples J, Matthews S, Heemstra S, Price O, Badlan R (2018) How do weather and terrain contribute to firefighter entrapments in Australia? *International Journal of Wildland Fire* **27**, 85–98. doi:10.1071/WF17114
- McGrattan K, Hostikka S, Forney G, McDermott R, Weinschenk C (2013) Fire Dynamics Simulator, User’s Guide, 6th edn (original version 2013, revised version 6.3.2 in 2015). NIST special publication 1019. National Institute of Standards and Technology. doi:10.6028/NIST.SP.1019
- McGrattan K, Hostikka S, McDermott R, Floyd J, Weinschenk C, Overholt K (2015) Fire Dynamics Simulator Technical Reference Guide Volume 1: Mathematical Model. NIST special publication 1018-1. National Institute of Standards and Technology. doi:10.6028/NIST.SP.1018
- Mell W, Jenkins MA, Gould J, Cheney P (2007) A physics-based approach to modelling grassland fires. *International Journal of Wildland Fire* **16**, 1–22. doi:10.1071/WF06002
- Mell W, Maranghides A, McDermott R, Manziello SL (2009) Numerical simulation and experiments of burning Douglas fir trees. *Combustion and Flame* **156**, 2023–2041. doi:10.1016/j.combustflame.2009.06.015
- Mell W, Simeoni A, Morvan D, Hiers JK, Skowronski N, Hadden RM (2018) Clarifying the meaning of mantras in wildland fire behaviour modelling: reply to Cruz et al. (2017). *International Journal of Wildland Fire* **27**, 770–775. doi:10.1071/WF18106
- Mendes-Lopes JMC, Ventura JMP, Amaral JMP (2003) Flame characteristics, temperature–time curves, and rate of spread in fires propagating in a bed of *Pinus pinaster* needles. *International Journal of Wildland Fire* **12**, 67–84. doi:10.1071/WF02063
- Moinuddin KAM, Sutherland D, Mell W (2018) Simulation study of grass fire using a physics-based model: striving towards numerical rigour and the effect of grass height on the rate-of-spread. *International Journal of Wildland Fire* **27**, 800–814. doi:10.1071/WF17126
- Morandini F, Silvani X, Dupuy J-L, Susset A (2018) Fire spread across a sloping fuel bed: Flame dynamics and heat transfers. *Combustion and Flame* **190**, 158–170. doi:10.1016/j.combustflame.2017.11.025
- Morvan D, Frangieh N (2018) Wildland fires behaviour: wind effect versus Byram’s convective number and consequences upon the regime of propagation. *International Journal of Wildland Fire* **27**(9), 636–641. doi:10.1071/WF18014
- Perez-Ramirez Y, Mell WE, Santoni PA, Tramoni JB, Bosseur F (2017) Examination of WFDS in modeling spreading fires in a furniture calorimeter. *Fire Technology* **53**(5), 1795–1832. doi:10.1007/s10694-017-0657-z
- Sánchez-Monroy X, Mell W, Torres-Arenas J, Butler BW (2019) Fire spread upslope: Numerical simulation of laboratory experiments. *Fire Safety Journal* **108**, 102844. doi:10.1016/j.firesaf.2019.102844
- Sharples JJ (2017) Risk implications of dynamic fire propagation. A case study of the Ginninderry region. Preliminary Report, June 2017. (Prepared for Ginninderry Falls Association)
- Sharples JJ, Viegas DX, McRae RHD, Raposo JRN, Farinha HAS (2011) Lateral bushfire propagation driven by the interaction of wind, terrain and fire. In ‘19th International Congress on Modelling and Simulation’, Perth, Australia, 2011. pp. 12–16. Available at <https://www.mssanz.org.au/modsim2011/A2/sharples.pdf>
- Sutherland D, Sharples JJ, Moinuddin KAM (2020) The effect of ignition protocol on grassfire development. *International Journal of Wildland Fire* **29**, 70–80. doi:10.1071/WF19046
- Sutherland D, Sharples JJ, Moinuddin K (2022) Simulated flame shape and heat transfer of quasi-equilibrium grass fire at transitional Byram numbers. In ‘Advances in Forest Fire Research 2022’. (Eds DX Viegas, LM Ribeiro) pp. 767–774. (University of Coimbra: Portugal)
- Tang W, Gorham DJ, Finney MA, McAllister S, Cohen J, Forthofer J, Gollner MJ (2017) An experimental study on the intermittent extension of flames in wind-driven fires. *Fire Safety Journal* **91**, 742–748. doi:10.1016/j.firesaf.2017.03.030
- Viegas DX (2004) A mathematical model for forest fires blowup. *Combustion Science and Technology* **177**, 27–51. doi:10.1080/00102200590883624

Data availability. The data that support this study will be shared on reasonable request to the corresponding author.

Conflicts of interest. The authors declare no conflict of interest in this study.

Declaration of funding. This research was supported by the Bushfire and Natural Hazards Cooperative Research Centre project: ‘Fire spread prediction across fuel types’.

Author affiliations

^AInstitute for Sustainable Industries and Liveable Cities, Victoria University, Melbourne, Australia.

^BBushfire and Natural Hazards Cooperative Research Centre (CRC), East Melbourne, Vic. 3002, Australia.

^CSchool of Science, University of New South Wales, Canberra, ACT 2610, Australia.